

Inactivation of Hedgehog signal transduction in adult astrocytes results in region-specific blood–brain barrier defects

Hui Wang^{a,b,1} , Zhiyan Xu^{a,b,1} , Ziyue Xia^{a,b}, Michael Rallo^b , Andrew Duffy^b, and Michael P. Matise^{b,2}

^aDepartment of Pharmacology, School of Pharmacy, Nantong University, Nantong 226001, China; and ^bDepartment of Neuroscience and Cell Biology, Robert Wood Johnson Medical School, Rutgers Biomedical and Health Sciences, Piscataway, NJ 08854

Edited by Chenchua Gu, Harvard University, Cambridge, MA, and accepted by Editorial Board Member Jeremy Nathans July 14, 2021 (received for review August 24, 2020)

In this study, we use molecular genetic approaches to clarify the role of the Hedgehog (Hh) pathway in regulating the blood–brain/spinal cord barrier (BBB) in the adult mouse central nervous system (CNS). Our work confirms and extends prior studies to demonstrate that astrocytes are the predominant cell type in the adult CNS that transduce Hh signaling, revealed by the expression of *Gli1*, a target gene of the canonical pathway that is activated in cells receiving Hh, and other key pathway transduction components. *Gli1*+ (Hh-responsive) astrocytes are distributed in specific regions of the CNS parenchyma, including layers 4/5/6 of the neocortex, hypothalamus, thalamus, and spinal cord, among others. Notably, although BBB properties in endothelial cells are normally regulated by both paracellular and transcellular mechanisms, conditional inactivation of Hh signaling in astrocytes results in transient, region-specific BBB defects that affect transcytosis but not paracellular diffusion. These findings stand in contrast to prior studies that implicated astrocytes as a source of Sonic hedgehog that limited extravasation via both mechanisms [J. I. Alvarez et al., *Science* 334, 1727–1731 (2011)]. Furthermore, using three distinct Cre driver lines as well as pharmacological approaches to inactivate Hh-pathway transduction globally in CNS astrocytes, we find that these specific BBB defects are only detected in the rostral hypothalamus and spinal cord but not the cortex or other regions where *Gli1*+ astrocytes are found. Together, our data show that *Gli1*+ Hh-responsive astrocytes have regionally distinct molecular and functional properties and that the pathway is required to maintain BBB properties in specific regions of the adult mammalian CNS.

sonic hedgehog | astrocyte | blood–brain barrier | albumin extravasation | transcytosis

Maintenance of the blood–brain/spinal cord barrier (BBB) in the mammalian central nervous system (CNS) is an active, ongoing process involving interactions between blood vessel endothelial cells (ECs) and several types of perivascular cells, including mural cells, such as pericytes, which are primarily associated with capillaries, and astrocytes, which extend processes that end in enlargements (endfeet) that contact ECs. Astrocytes, together with pericytes, play a pivotal role in establishing the BBB during development and maintaining the BBB in adults via secretion of basal lamina and signaling factors that control CNS EC-specific properties (1–7). Among these properties are the presence of specialized tight junction (TJ) proteins that restrict paracellular diffusion between ECs and low rates of transcytosis compared to peripheral vessels. Astrocytes have also been shown to be key players in repairing BBB disruptions that are associated with CNS injuries or neurological disorders (1, 3–5, 7–12). Recent studies have demonstrated that astrocytes are a heterogeneous population of cells with distinct molecular signatures and unique responses to different injuries or insults (13–21). However, it is unclear whether distinct subsets of astrocytes located in different regions of the CNS play unique or different roles in influencing BBB properties.

A number of studies have begun to reveal the potential mechanisms employed by perivascular astrocytes in maintaining BBB integrity. Several signaling molecules have been implicated in this process, including those of the Wnt and Sonic hedgehog (Shh) pathways (6, 22, 23). In the case of the latter pathway, it has been proposed that Shh is produced by resting CNS astrocytes and signals to ECs to induce specific TJ proteins involved in restricting paracellular diffusion (6). However, more recent transcriptome studies, including the present work, have clearly demonstrated that astrocytes, and not ECs, are the primary postmitotic cell type that are responding to Hedgehog (Hh) signaling in the adult brain, and furthermore have failed to corroborate the expression of Shh within resting astrocytes. Thus, the role of this pathway in BBB regulation remains undefined.

In this study, we addressed this issue using molecular genetic approaches to clarify the role of the Hh pathway in regulating the BBB in the adult mouse CNS. Our work confirms and extends earlier published studies to unequivocally demonstrate that astrocytes are the predominant differentiated cell type in the adult CNS that transduce Hh signaling. *Gli1*+ (Hh-responsive) astrocytes are distributed in specific regions of the CNS parenchyma (gray matter), including layers 4/5/6 of the neocortex, hypothalamus, thalamus, and spinal cord, among others (24, 25) (also see *Results*). Notably, we find that conditional inactivation

Significance

Several signaling pathways have been implicated in regulating blood–brain/spinal cord barrier (BBB) properties in the adult mammalian central nervous system (CNS). However, it has become clear that the role of the Sonic hedgehog pathway has not been accurately defined. The current work addresses this issue by demonstrating that the pathway is required in protoplasmic astrocytes to maintain specific BBB characteristics in select regions of the CNS. In contrast to prior studies, we find that astrocytic, and not endothelial cell, Hedgehog signal transduction is required to maintain BBB properties through an effect on transcytosis but not paracellular diffusion. Our discovery raises the possibility that targeted inhibition of the pathway to achieve transient BBB permeability could be exploited for therapeutic purposes.

Author contributions: M.P.M. designed research; H.W., Z. Xu, Z. Xia, M.R., and A.D. performed research; M.P.M. analyzed data; and M.P.M. wrote the paper.

The authors declare no competing interest.

This article is a PNAS Direct Submission. C.G. is a guest editor invited by the Editorial Board.

Published under the PNAS license.

¹H.W. and Z. Xu contributed equally to this work.

²To whom correspondence may be addressed. Email: matisemp@rwjms.rutgers.edu.

This article contains supporting information online at <https://www.pnas.org/lookup/suppl/doi:10.1073/pnas.2017779118/-DCSupplemental>.

Published August 20, 2021.

of Hh signal transduction in adult astrocytes results in transient, region-specific BBB defects that affect transcytosis but not paracellular diffusion. Furthermore, using three distinct Cre driver lines to inactivate Hh-pathway transduction globally in CNS astrocytes, we find that these specific BBB defects are only detected in the rostral hypothalamus and spinal cord but not the cortex or other regions where Gli1+ astrocytes are found. Together, these data show that Gli1+ Hh-responsive astrocytes have regionally distinct molecular and functional properties and also reveals that the pathway is required to maintain BBB properties in specific regions of the adult mammalian CNS.

Results

Hh-Responsive Gli1+ Protoplasmic Astrocytes Have a Regionally Distinct Expression Profile and Distribution and Are Associated with Blood Vessels. Hh-responsive cells can be identified by their expression of *Gli1*, a target gene and effector of the pathway that is activated in cells receiving signaling. Gli1+ (expressing) cells are distributed in many regions of the mammalian CNS, including progenitor cells located in the germinal zones in the brain (subventricular zone [SVZ] and subgranular zone [SGZ]) (26, 27) and postmitotic astrocytes located in the gray matter (24) (Fig. 1A and *SI Appendix, Fig. S1 A–D*). In the brain, Gli1+ astrocytes show a region-specific distribution, including layers 4/5/6 of the somatosensory (*SI Appendix, Fig. S1A*), motor, cingulate and association cortices, globus pallidus (*SI Appendix, Fig. S1B*), hypothalamus (*SI Appendix, Fig. S1C*), thalamus, hippocampus, septum, substantia nigra, brainstem, cerebellum, and a few other regions. A few scattered Gli1+ cells can also be seen in cortical layers 2/3. Prior studies have found that Gli1+ astrocytes represent about 1/4 of all astrocytes in the cortex, while in the globus pallidus and hypothalamus, the proportion is between 50% and 80%, respectively (24).

Prior studies have shown that Gli1+ expression in the postnatal brain is largely, if not entirely, confined to astrocytes. To evaluate whether this also applies to the spinal cord, we carried out both immunohistochemical and bulk transcriptome analysis of fluorescent-activated cell sorting–isolated Gli1+ (GFP+ or TdTomato [TdT] +) spinal cord cells. In the spinal cord, expression is confined to a stable population of nondividing protoplasmic gray matter astrocytes comprising ~31% of Sox9-expressing cells, and these are distributed in the dorsal, intermediate, and ventral horns at all axial levels, with a somewhat higher number in the dorsal horn (Fig. 1A and *SI Appendix, Figs. S1–S3 and Table S1*). RNA sequencing (RNAseq) analysis revealed that Hh-pathway transduction components are significantly enriched in Gli1+ spinal cord cells compared to other Gli1– (GFP– or TdT–) cell types (Fig. 1C and D).

We also compared Hh transduction components between Gli1+ spinal cord and cortical cells. In both regions, Gli1+ cells show enrichment for *Gli1* and *Ptch1*, two target genes of the pathway. *Gli1* expression is only seen in cells that are actively transducing canonical Hh signaling, while *Ptch1* levels are up-regulated in responding cells. Notably, both *Gli2* and *Gli3* were also enriched, but not *Shh*, which was not detected. Together, these data indicate that these cells are capable of transducing Hh signaling but do not themselves express ligand under normal resting conditions (Fig. 1D). Notably, cortical astrocytes show a unique enrichment of *Boc* and *Gas1*, two genes involved in modifying the sensitivity of responding cells to Hh ligands (Fig. 1D) (28, 29). This may reflect a difference in the manner in which Hh ligands activate the pathway in competent cells in different regions of the CNS (30). Overall, these data are in good agreement with numerous independently published studies characterizing the transcriptome of CNS cells (13–21) and, taken with immunohistochemical studies, confirm and extend data indicating that Gli1+ astrocytes are the predominant differentiated cell type in the normal adult mouse CNS that is actively responding to canonical Hh signaling, although there

appear to be some regional differences in the expression of specific pathway components.

Finally, confocal analysis of Gli1+ astrocyte processes shows that Gli1+ astrocytes make contact with ECs in both the brain (hypothalamus and cortex) and spinal cord, although only a subset of blood vessels are associated with Gli1+ endfeet in these regions (Fig. 1B–B' and *SI Appendix, Fig. S4*). We have not established whether all Gli1+ astrocytes make contact with blood vessels.

Genetic Inactivation of Hh Signal Transduction in Gli1+ Astrocytes Results in Albumin Extravasation.

To test the possibility that Hh signaling in Gli1+ astrocytes is important for maintaining BBB properties, we used conditional mutagenesis to inactivate Hh signal transduction selectively in astrocytes in adult (>P30) mice using several approaches and assayed BBB integrity in regions of the CNS where they are located. We first asked whether *Gli1* itself was required to maintain the fate of these cells by examining *Gli1* reporter gene expression, cell fate (by scoring Sox9 coexpression), or bromodeoxyuridine (BrdU) incorporation in adult homozygote *Gli1^{lacZ/lacZ}* and *Gli1-Cre^{ERT2/ERT2};Rosa^{eYFP}* mice (both *Gli1^{+/+}*) compared to *Gli1^{lacZ/+}* and *Gli1-Cre^{ERT2/+}* heterozygotes. We found no differences between *Gli1* mutant and heterozygous mice at P60 or P360 (*SI Appendix, Fig. S3*), indicating that *Gli1* is not required downstream of Hh signaling to maintain pathway activation (revealed by persistent *Gli1* expression) or astrocyte identity (i.e., all Gli1+ astrocytes colabel with Sox9 at both P60 and P360). Finally, GFAP levels, determined by antibody staining in tissue sections, were similar between *Gli1^{+/+}* and *Gli1^{+/+}* mice, indicating that reactive gliosis is not elicited in the absence of *Gli1* (*SI Appendix, Fig. S3 C and D*). Although these data do not rule out a subtle role for *Gli1*, they are consistent with numerous other studies that demonstrate that this factor is functionally redundant with Gli2 and Gli3 in mice in multiple contexts, both of which are coexpressed with Gli1 in CNS astrocytes (Fig. 1C and D) (31–33).

To determine the requirement of Hh signaling in Gli1+ cells, we generated *Gli1-Cre^{ERT2/+};Rosa26^{eYFP/+};Smo^{c/c}* mice containing a floxed *Smo* allele (34). To inactivate Hh signal transduction specifically in adult Gli1+ cells, *Gli1-Cre^{ERT2/+};Rosa^{eYFP};Smo^{c/c}* and *Gli1-Cre^{ERT2/+};Rosa^{eYFP}* (control) mice were collected at five time points after a single tamoxifen (TAMX) injection at P35 to P45 and processed for Evans Blue (EB) extravasation analysis in whole spinal cord, whole brain, and liver (internal control) tissue extracts to indirectly monitor serum albumin infiltration into the CNS. We found a significant increase in EB levels in spinal cord tissue from *Smo^{+/+}* mutant mice versus controls at 0.5 d, 1 d (24 h), and 2 d, and a smaller but still significant increase in brain tissue at 1 and 2 d after TAMX injection (*SI Appendix, Fig. S5B*). EB could also be detected in spinal cord tissue sections 1 d after TAMX treatment (*SI Appendix, Fig. S5 C and D*). Interestingly, both spinal cord and brain EB returned to control levels at 3 d following TAMX and persisted at that level at the latest time point analyzed (7 d) (*SI Appendix, Fig. S5B*), indicating that the defect is transient.

BBB Disruption Affects Endocytosis/Transcytosis but Not Paracellular Diffusion.

To determine the requirement for Hh signal transduction specifically in astrocytes, we used two different transgenic Cre driver lines to inactivate *Smo* in these cells: *Gfap-Cre^{ERT2}* (35, 36) and *Aldh1l1-Cre^{ERT2}* (37). These lines allowed us to maximize the recombination/inactivation of *Smo* by administering multiple TAMX injections over several days, as neither the *Gfap-Cre^{ERT2}* nor *Aldh1l1-Cre^{ERT2}* drivers depend on Hh signal transduction for their expression. We first confirmed overlap of *Gfap*-driven Cre-recombinase expression in Gli1+ cells by examining colabeling in *Gfap-Cre^{ERT2/+};Rosa^{TdT/TdT};Gli1^{lacZ/+}* mice, where TdT expression is driven by *Gfap* and β-gal by *Gli1* (from one allele) on day 4 following 3 successive days of TAMX administration. We found significant and extensive TdT (Gfap) expression in Gli1+ (β-gal+)

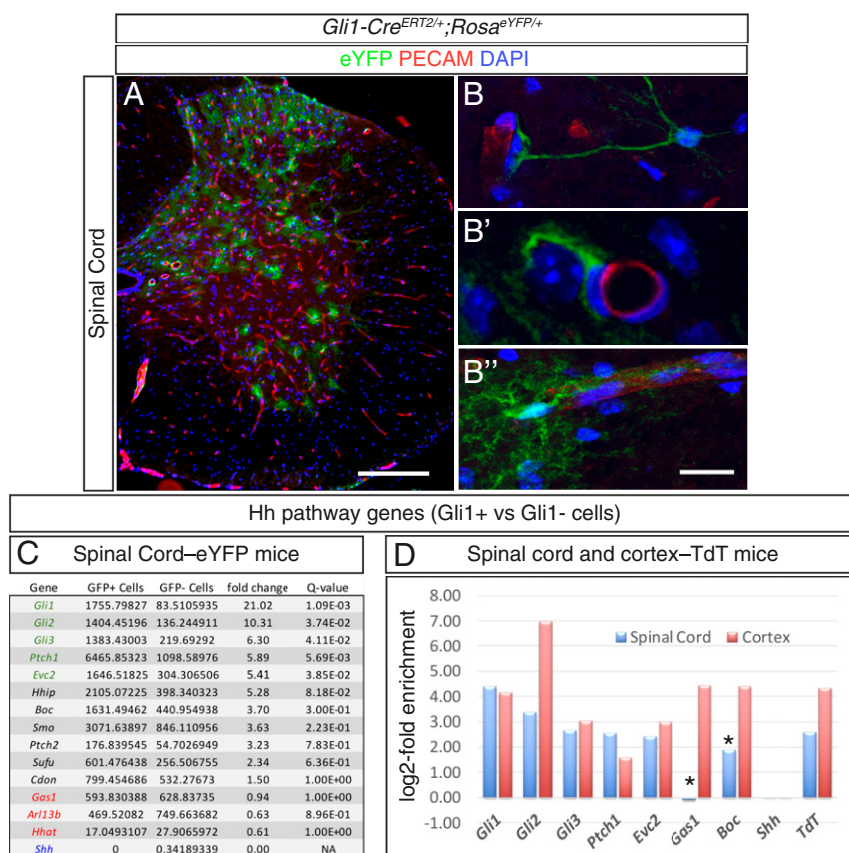


Fig. 1. Characterization of Gli1+ cell identity and cell process contacts. (A) eYFP expression in the spinal cord of P35 to P42 *Gli1-Cre^{ERT2/+};Rosa26^{eYFP/YFP}* mice given three doses of TAMX daily beginning at P30 and collected 7 d later. eYFP expression is confined to astrocytes located in the gray matter. (B–B'') The 60× confocal images show that many eYFP+ (Gli1+) astrocytes project endfeet to contact blood vessels. PECAM marks blood vessels in all panels. (C) Table lists Hh-pathway transduction genes from *Gli1-Cre^{ERT2/+};Rosa26^{eYFP/YFP}* mice given TAMX as described. Genes in green text indicate those that are significantly enriched in the sorted GFP+ versus GFP- populations (Q-value ≤ 0.05), while those in red are significantly down-regulated. (D) Chart compares significantly enriched Hh-pathway transduction genes in Tdrt+ versus Tdrt- cells purified from spinal cord (blue columns) and cortex (red) from *Gli1-Cre^{ERT2/+};Rosa26^{Tdrt/Tdrt}* mice injected with TAMX at P30 as described, plotted as log2-fold enrichment. Similar enrichment is seen for the listed genes in both regions except those indicated by an asterisk, which are not significantly enriched in spinal cord samples. Tdrt serves as a positive control for this data. Note that *Shh* is not detected in the data sets for experiments shown in both C and D. (Scale bar in A, 200 μm; in B'', 15 μm for B and B'' and 25 μm for B''')

cells throughout the hypothalamus, an area with a high concentration of Gli1+ astrocytes and dense blood vessel networks, and gray matter of the spinal cord, but essentially no coexpression in cortical cells (SI Appendix, Fig. S6). Thus, we focused our analysis on the former two structures in subsequent experiments with this line.

We injected Alexa488-conjugated albumin (albumin-488) or tetramethylrhodamine-conjugated biocytin (biocytin-TMR) into the tail vein of *Gfap-Cre^{ERT2/+};Smo^{c/c}* and control (*Gfap-Cre^{ERT2/+}* only) mice to assay transcytosis and paracellular BBB integrity, respectively, 1 d after administering TAMX for 3 successive days, as discussed previously. We found a significant accumulation of albumin-488 in both rostral hypothalamic (Fig. 2A–E) and spinal cord (Fig. 2F and SI Appendix, Fig. S7) blood vessel walls in *Smo^{-/-}* mutant tissue compared to controls (white arrowheads). Notably, some of the albumin-488 tracer could also be seen in the parenchyma in the paraventricular nucleus (PVN) region of the anterior hypothalamus, but not spinal cord, in *Smo^{-/-}* mutants (Fig. 2C–C'', yellow arrowheads, and SI Appendix, Fig. S7). Examination of PVN blood vessels by scanning transmission electron microscopy showed a substantial increase in the number of endocytic vesicles and mitochondria in ECs in *Smo^{-/-}* versus control tissues (Fig. 3A–B'''). These data indicate that bulk transport of albumin into PVN ECs is increased in mice where *Smo* has been inactivated in hypothalamic astrocytes. Consistent with this, we also detected elevated levels of

Caveolin-1 protein, a marker for vesicle-mediated bulk transport across brain ECs, in both spinal cord and diencephalic (hypothalamus/thalamus) tissue extracts of mice treated with the same TAMX protocol as discussed previously compared to control (SI Appendix, Fig. S84), where the level of this protein is typically low, consistent with the reduced levels of transcytosis in the CNS.

In contrast to these findings, we did not detect extravasation of injected biocytin-TMR (molecular weight [MW] = 869 Da) or plasma fibrinogen in the brain (Fig. 4 and SI Appendix, Fig. S9) in *Gfap-Cre^{ERT2};Smo^{c/c}* mice, indicating an intact paracellular boundary. Consistent with this, analysis of TJ proteins Claudin-5, Occludin, and ZO-1 did not reveal alterations in their continuity (EC TJ contacts) in the brain or changes in the levels of these proteins in the spinal cord or diencephalon of these mice (SI Appendix, Figs. S10 and S11), a phenotype often associated with paracellular boundary disruption. To rule out more subtle defects in paracellular boundary integrity, we examined extravasation of sodium fluorescein (NaF; MW = 376 Da) in *Gfap-Cre^{ERT2};Smo^{c/c}* mice and did not detect any infiltration into the CNS in the rostral hypothalamus (SI Appendix, Fig. S12A–B'''). Similarly, we did not detect any gaps in TJ contacts between ECs in *Smo^{-/-}* mice at the electron microscopy (EM) level (Fig. 3A and B). These data support tracer injection data indicating that TJ continuity or protein levels are not affected in *Gfap-Cre^{ERT2};Smo^{c/c}* mice.

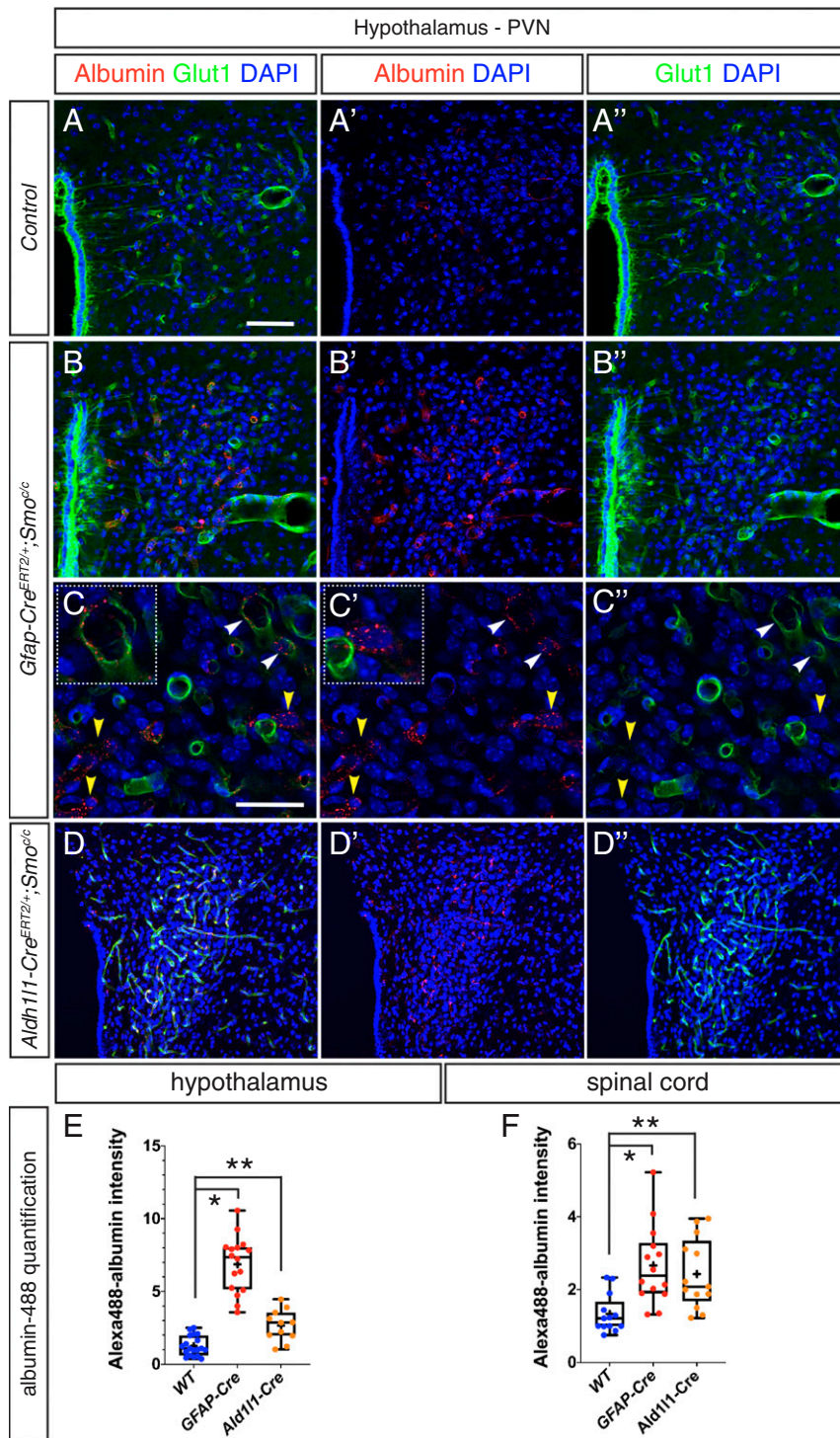


Fig. 2. Albumin extravasation in the CNS of mice with conditional inactivation of *Smo* in astrocytes. (A) Coronal sections through the rostral hypothalamus at the PVN level in *Gfap-Cre^{ERT2/+}; Smo^{-/-}* mice reveal that alexa488-albumin tracer can be detected in close association with Glut1+, a marker for blood vessels (B–B'') as well as in the parenchyma (C–C'', insets) (i.e., not associated with blood vessels) compared to control injected mice (A–A''). White arrowheads in C–C'' indicate blood vessels, while yellow arrowheads indicate parenchymal (non-blood vessel associated), albumin accumulation. (D–D'') Sections through the rostral hypothalamus in *Aldh111-Cre^{ERT2/+}; Smo^{-/-}* mice show a similar pattern of albumin leakage. (E and F) Quantification of albumin leakage using fluorescent intensity measurements in the hypothalamus (E) and spinal cord (F) of *Gfap-Cre^{ERT2/+}; Smo^{-/-}* (red dots) and *Aldh111-Cre^{ERT2/+}; Smo^{-/-}* mice (orange dots) compared to control (blue dots). *P* values in E: **P* < 0.0001; *P* values in F: **P* = 0.0005; ***P* = 0.0001 (Student's *t* test) comparing *Smo^{-/-}* to WT for each experiment. *n* = 5 experimental and control animals for *Gfap-Cre^{ERT2/+}; Smo^{-/-}* and *n* = 3 for *Aldh111-Cre^{ERT2/+}; Smo^{-/-}*. Error bars = SD. A–B'', D–D'' taken at 20×; C–C'' taken at 60×. (Scale bar in A, 100 μm for A–B'' and D–D''; Scale bar in C, 30 μm for C–C'').

To determine whether the increase in transcytosis in *Gfap-Cre^{ERT2}; Smo^{c/c}* mice was correlated with changes in pericyte coverage of blood vessels in the rostral hypothalamus, we examined

spatial expression of *Pdgfr-β* protein using immunohistochemistry and overall tissue levels using Western blotting in tissue extracts of *Smo^{-/-}* compared to control mice. We found that neither pericyte

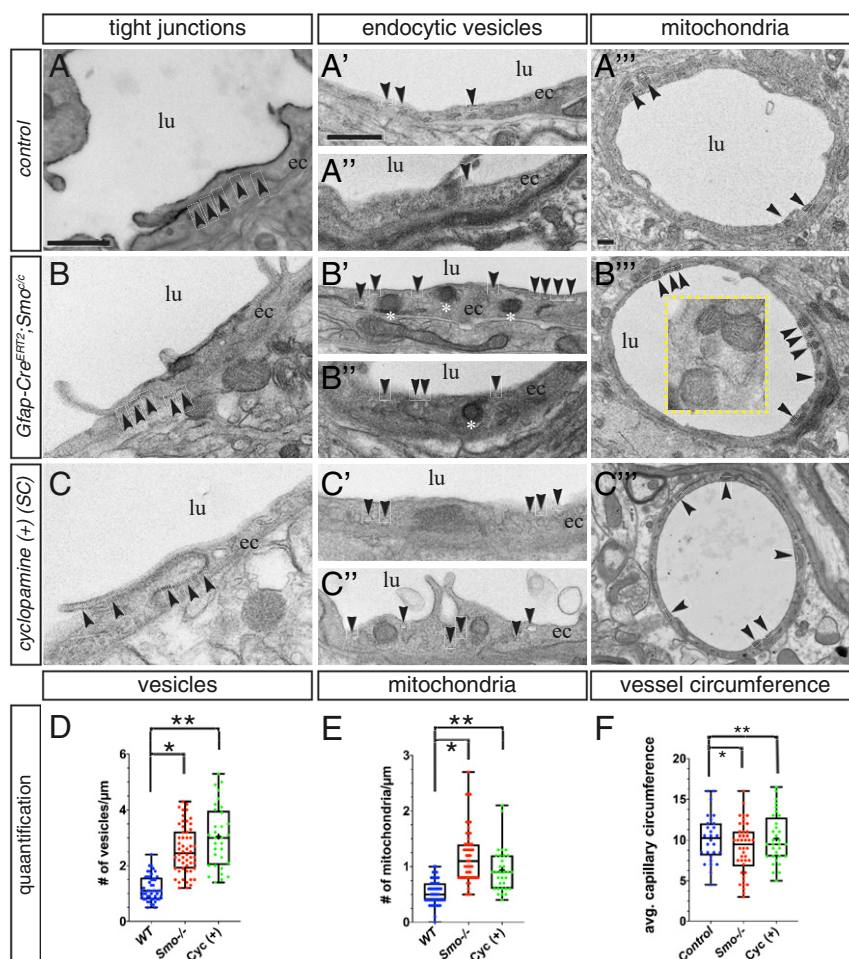


Fig. 3. Electron micrographs from mice with genetic or pharmacologic inactivation of *Smo*. (A–C'') Images through the rostral hypothalamus in WT and *Gfap-Cre^{ERT2/+};Smo^{-/-}* mice. TJ morphology is not interrupted in *Gfap-Cre^{ERT2/+};Smo^{-/-}* mice compared to control (arrowheads in A and B). Increased number of endocytic vesicles (A', A'', B', and B'', arrowheads) and mitochondria (A''' and B'', arrowheads) are seen in *Gfap-Cre^{ERT2/+};Smo^{-/-}* mice compared to controls. Inset in F shows higher magnification of mitochondria from a different image. (C–C'') TJ, vesicles, and mitochondria in the spinal cord of cyc-treated mice. (D and E) Quantification of number of vesicles and mitochondria per lineal micron in WT (blue dots), *Gfap-Cre^{ERT2/+};Smo^{-/-}* (*Smo^{-/-}*) (red dots) and cyc-treated (Cyc+) (green dots) mice. Error bars show SD. *, ** $P \leq 0.0001$ (Student's *t* test) for experimental compared to control mice. (F) Comparison of average circumference of imaged vessels for all three conditions in microns. No differences were seen between experimental and control vessel diameters (* $P = 0.1142$; ** $P \leq 0.4338$). $n = 3$ animals for each experiment. (Scale bars, 500 nm [bar in A applies to A–C, bar in A' applies to A'–C'', and bar in A''' applies to A'''–C''']). Abbreviations: lu = lumen, ec = endothelial cell.

coverage of blood vessels nor overall protein levels in *Smo^{-/-}* mutant PVN differed from controls (SI Appendix, Figs. S8B and S13B), suggesting that pericytes are not overtly affected. Overall, these data indicate that selective inactivation of Hh signal transduction in protoplasmic astrocytes results in loss of BBB integrity that is attributable to defects in endocytosis/transcytosis but not paracellular diffusion.

Since the *Gfap-CreERT2* line does not drive Cre-recombinase expression in *Gli1^{lacZ}* cells in the cortex (as measured by coexpression with *Gli1^{lacZ}*) and possibly other regions and is also expressed in some progenitors (36), we generated *Aldh1l1-CreERT2;Smo^{c/c}* mice, which employ a promoter/enhancer that has been shown to drive widespread robust expression specifically in CNS astrocytes (37). We examined BBB integrity in the brain and spinal cord in this line using a similar approach as previously discussed (two TAMX injections at >P35 mice, followed by collection 1 d later). We found a significant accumulation of albumin-488 in rostral hypothalamus and spinal cord (Fig. 2 D–F and SI Appendix, Fig. S7 D–D') but not cortical (SI Appendix, Fig. S7 E and E') blood vessel walls in *Smo^{-/-}* mutant tissue compared to controls, a similar regional extravasation

pattern as seen in *Gfap-CreERT2;Smo^{c/c}* mice (although the overall levels of albumin-488 were somewhat lower). In addition, neither biocytin-TMR nor NaF extravasation was detected in the hypothalamus in this line (Fig. 4 C–C'' and SI Appendix, Fig. S12 C–C''). Consistent with this, we did not detect any changes in pericyte coverage (SI Appendix, Fig. S13C) or TJ protein expression levels in either the spinal cord or diencephalon (SI Appendix, Fig. S14).

Finally, to determine whether the specific pattern of BBB disruption seen in *Gfap-CreERT2;Smo^{c/c}* or *Aldh1l1-CreERT2;Smo^{c/c}* mice was attributable to differences in Cre activity or *Smo* recombination efficiency in different CNS regions, we took two approaches. We generated a dual-color Rosa reporter line, *Gfap-CreERT2;Rosa^{GFP/TdT}*, to indirectly measure *Gfap* promoter-drive Cre activity and allelic recombination efficiency in various CNS regions. In these experiments, the frequency of recombination at one or both target Rosa alleles can be determined by examining whether GFP (green channel), TdT (red channel), or both (yellow) are detected, indicating recombination at one or both target alleles. We found that the proportion of yellow cells in six different CNS regions was similar (between 46% and 61%), indicating that

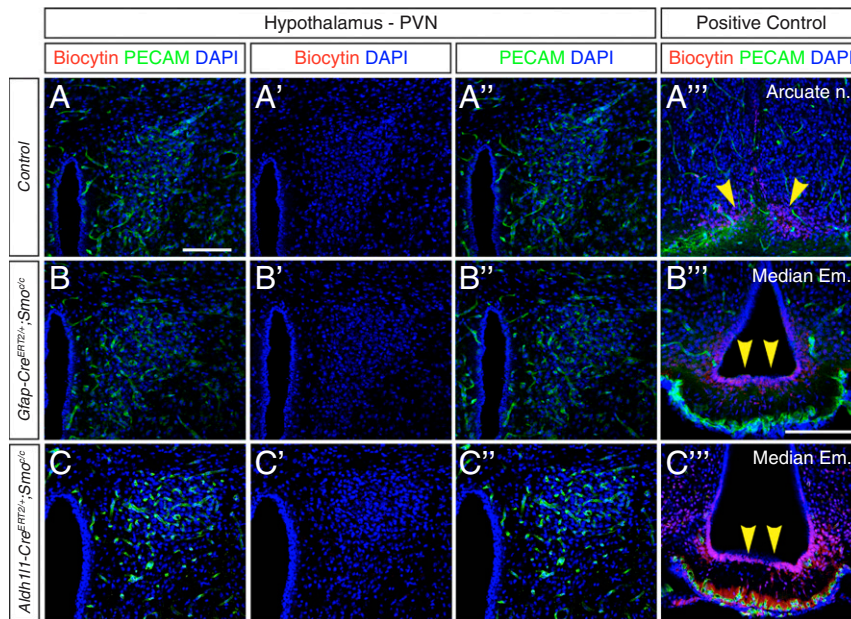


Fig. 4. The paracellular diffusion boundary is intact in *Smo*^{-/-} mice. (A–B'') Coronal sections through the rostral hypothalamus in mice injected with biocytin-TMR tracer. No tracer was detected in the parenchyma of *Gfap-Cre*^{ERT2/+}; *Smo*^{-/-} (B–B'') or *Aldh111-Cre*^{ERT2/+}; *Smo*^{-/-} (C–C'') mice, similar to controls (A–A''). (A''', B''', and C''') Extravasation of biocytin-TMR in the circumventricular organs of the brain (arcuate nucleus [n.] and median eminence [em.]) serves as an internal positive control for these experiments (yellow arrowheads). *n* ≥ 5 animals for experimental and control. (Scale bars, 100 μm [bar in B''' applies to B''' and C''']).

differences in Cre expression cannot explain regional BBB leakage patterns in this line (*SI Appendix, Fig. S15*). We also used qRT-PCR to examine *Smo* recombination efficiency in the cortex, spinal cord, and diencephalon (containing the rostral hypothalamus) in *Aldh111-Cre*^{ERT2/+}; *Smo*^{c/c} mice. In this line, Cre activity is widespread throughout all CNS regions but BBB defects only arise in the spinal cord and diencephalon when it is used to conditionally inactivate *Smo*, a similar regional pattern to *Gfap-Cre*^{ERT2/+}; *Smo*^{c/c} mice. We found that *Smo* expression was reduced by 48% and 55% in all three regions (*SI Appendix, Fig. S16*). Together, these data reveal that global inactivation of *Smo* in CNS astrocytes elicits a region-specific defect in BBB integrity that affects transcytosis but not paracellular diffusion.

Pharmacological Inhibition of *Smo* Activity with Cyclopamine Results in BBB Disruption in the Spinal Cord but Not Brain. We next took a pharmacologic approach to inactivating *Smo* by administering cyclopamine (cyc), a potent *Smo* antagonist (38), to C57BL/6, *Gli1*^{lacZ/+}, or *Gli1-Cre*^{ERT2/+}; *RosaTdT* mice. Systemic administration of low-dose (5 mg/kg body weight) cyc to P30 *Gli1*^{lacZ/+} mice resulted in a partial inhibition of β-gal expression in the spinal cord 24 h later (*SI Appendix, Fig. S17 A and A'*). At higher doses (20 mg/kg), we found that β-gal expression was drastically reduced and *Gli1* messenger RNA levels were nearly completely abolished in spinal cord, diencephalon, and cortex extracts (*SI Appendix, Fig. S17 A'' and B*). Notably, TdT reporter expression was still robustly detected in *Gli1-Cre*^{ERT2/+}; *RosaTdT* mice treated with high-dose cyc, and the number of TdT+ cells was not altered, indicating that *Gli1*+ astrocytes do not undergo apoptosis under conditions of *Smo* inactivation (*SI Appendix, Fig. S17 C–E*). Thus, cyc can effectively block *Smo* activation of *Gli1* expression in a dose-dependent manner in all three brain regions.

To assay BBB integrity in mice treated with high-dose cyc to completely block *Smo* activity (as measured by *Gli1* expression), we used EB extravasation and tracer injection methods as previously discussed. EB levels in treated C57BL/6 mice were elevated relative to control at both 24 and 48 h in the spinal cord

following cyc administration (Fig. 5). Interestingly, and unexpectedly, no significant difference was noted in brain extracts (Fig. 5B) in contrast to genetic inactivation of *Smo*, which elicits rapid extravasation in this tissue (Fig. 2 and *SI Appendix, Fig. S5*). Consistent with this, albumin-488 was detected in association with ECs in the spinal cord but not rostral hypothalamus of cyc-treated mice, compared to controls (Fig. 5 C–D''). Furthermore, treated ECs exhibited higher numbers of endocytic vesicles and mitochondria compared to controls (Fig. 3 C–F). In the spinal cord, injected biocytin-TMR, NaF, and plasma fibrinogen were not detected in the parenchyma of treated mice (*SI Appendix, Figs. S12 D–D''' and S18*), and EC TJ protein expression and ultrastructural continuity under EM were similar to untreated controls (Fig. 3C and *SI Appendix, Figs. S19 and S20*). Cyc treatment of outbred *Gli1-Cre*^{ERT2/+}; *RosaTdT* mice produced similar patterns of albumin-488 extravasation (spinal cord but not brain), indicating that these effects are not due to strain differences. Together, these data reveal that pharmacologic inactivation of Hh signaling with high-dose cyc produces a similar BBB defect that affects endocytosis/transcytosis but not paracellular diffusion in the spinal cord but not brain.

Reactive Gliosis Is Not Elicited following *Smo* Inactivation in Mice with BBB Disruption. Previous reports indicate that inactivation of *Smo* in CNS astrocytes elicits up-regulation of GFAP expression, which is indicative of reactive astrogliosis (24). Reactive astrogliosis is a complex process that differs at the molecular genetic level for different inducers and in different regions of the CNS (15, 19, 39). Notably, certain products of reactive gliosis have been linked to disruption of the BBB (40, 41). To determine whether inactivation of Hh signaling using the *Gfap-Cre*^{ERT2} driver resulted in reactive gliosis, we assayed GFAP levels in different brain regions using immunohistochemistry and Western blotting. We found no differences in GFAP expression in *Gfap-Cre*^{ERT2/+}; *Smo*^{c/c} mice compared to *Gfap-Cre*^{ERT2/+} only (control) mice in either the spinal cord or diencephalon (containing the hypothalamus) (*SI Appendix, Fig. S8C*). Thus, although these data do not rule out more subtle

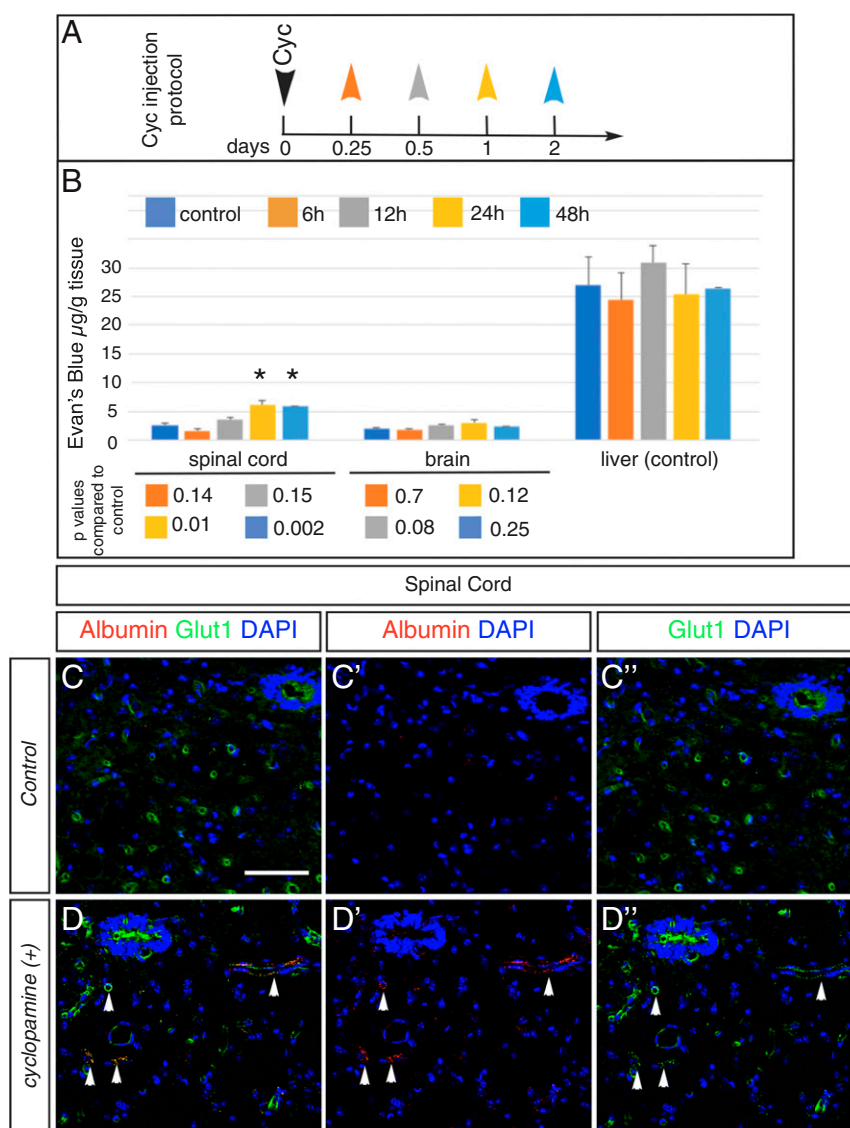


Fig. 5. Extravasation of EB in the spinal cord at various time points following a single administration of cyc in WT C57BL/6 mice. (A) Top panel illustrates cyc injection protocol showing the time points, indicated by different color arrowheads, at which tissue was harvested following a single dose. (B) Chart shows relative levels of EB in spinal cord and brain tissue harvested at the indicated time points. Asterisks indicate values that are significantly greater than control tissue, with corresponding *P* values shown below (Student's *t* test). Error bars = SD. (C and D) Albumin-488 extravasation in cyc-treated WT (C) and WT C57BL/6 mice (D) mouse spinal cords 24 h after cyc administration. Arrowheads in D–D'' indicate extravasated albumin-488. Albumin-488 intensity is significantly greater in cyc-treated versus control mice (*P* = 0.0003; Student's *t* test) (*n* = 6 animals each). (Scale bar, 50 μm .)

reactive changes, our results do not generally support the idea that global reactive gliosis, a process whose effects accumulate over time, can explain the rapid, transient increase in endocytosis/transcytosis that occurs in specific regions of the CNS following loss of Hh signal transduction in hypothalamic and spinal cord astrocytes.

Discussion

In this study, we show that astrocytes are the predominant differentiated cell type in the mature mouse CNS that are responding to ongoing canonical Hh signaling under normal conditions and that signal transduction in these cells is necessary to maintain normal BBB integrity in specific regions of the CNS. Together, our data clarify the influence of the Hh pathway on the BBB and reveal a region-specific dependency on signaling for maintaining its integrity (Fig. 6). These results raise the possibility that the transient effects of selective Hh-pathway inactivation in astrocytes could be exploited for clinical purposes

for the delivery of therapeutic compounds to specific regions of the CNS.

In adult mice, Hh-responsive *Gli1*⁺ astrocytes are found in specific regions of the CNS (24, 42), but they are not uniformly distributed among these areas. In some regions, like the hypothalamus, the majority of astrocytes appear to express *Gli1*, while in the cortex, a much smaller proportion express *Gli1*, and these are found largely (but not exclusively) in the middle and deeper cortical layers (24). This pattern suggests that there are distinct mechanisms for activating the canonical pathway in different regions, which could partially explain the distinct consequences resulting from its inactivation. In the spinal cord and cortex, transcriptome analysis of isolated *Gli1*-expressing cells shows that they share enrichment of the main core intracellular transduction components (*Ptch1*, *Gli2*, *Gli3*, *Gli1*) but differ in others that are involved in cell surface signal reception (*Gas1*, *Boc*), a discrepancy that is consistent with the possibility that there are

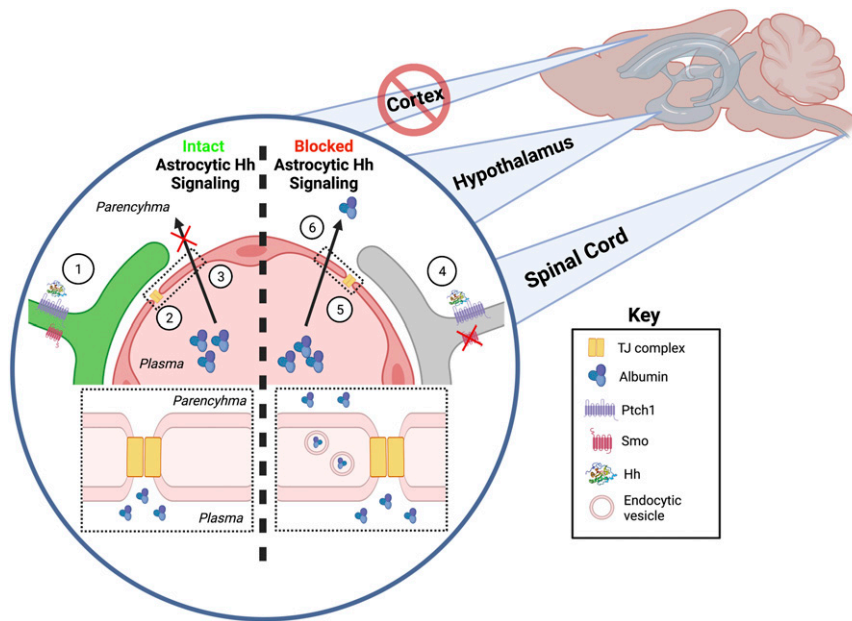


Fig. 6. Model illustrating the regional impact of inactivating Hh signaling in adult astrocytes on the BBB. (Left) Intact Hh signaling in astrocytes. (1) Binding of Shh to the Ptch1 receptor (purple) on astrocytes relieves inhibition on Smo (pink) and activates downstream Hh signaling targets, including *Gli1* (indicated by green astrocyte endfoot). (2) Intact TJ between ECs presents a physical barrier to the paracellular diffusion of plasma components into the CNS. (3) Transcytosis of plasma proteins (e.g., albumin; blue/purple bubbles) is suppressed in CNS ECs under normal conditions in comparison to peripheral vessels (see enlarged illustration). (Right) Blocked Hh signaling in astrocytes. (4) Genetic or pharmacologic inhibition of Smo in astrocytes prevents pathway activation and expression of downstream factors (i.e., *Gli1*) (indicated by gray astrocyte endfoot). (5) The paracellular TJ barrier remains intact in cells with blocked astrocytic Hh signaling. (6) Inhibition of astrocytic Hh signaling results in increased transcytosis (see enlarged illustration) and accumulation of plasma proteins in the CNS parenchyma of the hypothalamus and spinal cord but not the cortex. Image created with BioRender.com.

distinct ligand distribution and activation mechanisms in each region. It has been proposed that the CSF is a source of Shh that can activate the canonical pathway in SVZ progenitor cells (30), while neurons may be the source that activates the pathway in deeper cortical layers (24), although a relatively small number of neurons appear to express Shh compared to the large population of *Gli1*⁺ astrocytes in this structure. Although the source of ligand to activate *Gli1* expression in the hypothalamus, an area with a very high density of Hh-responsive astrocytes, has not been identified, it is also possible that Shh in the CSF of the III ventricle might serve this function given the close relationship that cells in the hypothalamus have with this structure, although this has not yet been shown. In contrast, the source of Hh ligand in the spinal cord is not likely solely derived from the CSF given the widespread distribution of *Gli1*⁺ cells in the gray matter and the limited amount of CSF present in the central canal, a ventricular structure that is much smaller than those found in the brain.

Prior studies have implicated Hh signaling in maintaining the BBB via a mechanism involving regulation of EC TJ protein expression by astrocyte-derived Shh ligand (43). In this model, astrocyte-secreted Shh binds to Ptch1 receptors expressed on ECs to activate Smo and initiate *Gli1* transcription and presumably other target genes, leading to the up-regulation of some TJ proteins that help restrict paracellular diffusion across the BBB into the CNS. Our astrocyte expression profiling results are corroborated by several independent transcriptome studies that together demonstrate that the core canonical Hh-pathway transduction components, including *Ptch1*, *Smo*, and *Gli* genes, are specifically expressed in protoplasmic astrocytes and not CNS ECs (13–21). Taken together, our data are incompatible with an astrocyte-to-EC Shh signaling model and instead implicate astrocytes as the primary Hh-responsive cell population in the normal CNS, and that signal reception in these cells, and not

ECs, is involved in regulating aspects of BBB permeability. Furthermore, our results also indicate a surprisingly limited effect of cyc on Hh signaling and BBB integrity in the brain versus the spinal cord despite the efficient inhibition of *Gli1* expression in both regions. While it is unclear why such a difference was seen, it is possible that the high levels of cyc necessary to achieve global inhibition of Smo in the CNS as well as the effect on other cell types in addition to astrocytes could produce complex side effects that attenuate, or otherwise compensate for, the effect in the rostral hypothalamus (44). This finding will present challenges for the design of pharmacologically based therapeutic approaches to exploiting the transient and specific effects that astrocyte-specific inactivation of Hh signaling could have for therapeutic purposes.

Materials and Methods

Mice. All mice were maintained in a specific pathogen free barrier facility and in conformation with institutional animal care and use committee guidelines. Individual *Gli1-Cre^{ERT2}*, *Gli1^{lacZ}*, *Smo^{fllox/fllox}* (*Smo^{fl}*), *Gfap-Cre^{ERT2}*, *Aldh1l1-Cre^{ERT2}*, *Rosa26^{eYFP}* (*R26R-EYFP*), and *Rosa26^{tdT}* (*Ai14*) mouse lines have been previously described (34–36, 45, 46). *Rosa26* reporter mice were obtained from the Jackson Laboratory; C57BL/6 mice were obtained from Charles River Laboratories. All combined genotype targeted/transgenic lines were maintained on an outbred background. All mice were analyzed at postnatal day (P) 35 to 42, except where noted.

Drug Administration. TAMX (20 mg/mL in corn oil) (TAMX) (Sigma-Aldrich) was administered via gavage feeding tube at 150 mg/kg body weight. Cyc (1 mg/mL in 45% 2-hydroxypropyl- β -cyclodextrin [HPBC]) (Sigma-Aldrich) was administered via intraperitoneal injection at 5 or 20 mg/kg body weight. An equal volume of vehicle-only solution HPBC (45% in phosphate-buffered saline [PBS]) was injected in control mice.

BBB Permeability Assays. For EB assays, P45 to P60 mice were first perfused with cold PBS, followed by 200 mg/kg body weight EB administered intraperitoneally 2 h prior to sacrificing and harvesting brain, spinal cord, and liver

(control) tissue. For Alexa488-albumin and biocytin-TMR (Invitrogen) permeability assays, 100 μ L of a 1% solution in PBS was injected into the tail vein in isoflurane-anesthetized mice. For NaF (Sigma-Aldrich), 100 μ L of a 10% solution in PBS was injected into the tail vein in isoflurane-anesthetized mice. Animals were killed 30 min later and processed for immunohistochemistry. Control mice also received TAMX injections. Experimental mice were excluded from analysis if tracer extravasation was not readily detected in the circumventricular organs (median eminence, arcuate) or choroid plexus.

Immunohistochemistry. Tissues were fixed in 4% paraformaldehyde for 4 h (brain) or 2 h (spinal cord) on a rotating platform at 4 °C and cryoprotected in 30% sucrose before embedding in opimal cutting temperature (OCT) compound. (Tissue-Tek). Coronal brain sections were cut at 50 μ m on a Microm cryostat and stored as floating sections at -20 °C in OCT. Spinal cord tissues were embedded in OCT and transverse sections cut at 20 μ m and mounted on Fisherbrand Superfrost Plus slides. The following antibodies were used at the indicated dilutions: rabbit anti-RFP (to detect TdT) (1:200, 600-401-379, Rockland); rabbit anti-GFP (1:1,000, ab13970, Abcam); rabbit anti-GFAP (1:400, Z0334, Dako); rat anti-PECAM (platelet endothelial cell adhesion molecule) (CD41) (1:150, MEC 13.3, BD Biosciences) (to mark blood vessels); rabbit anti-Caveolin1 (1:300, Ab18199, Abcam); rabbit anti-Glut-1 (1:200; RB-9052-P0, Thermo Fisher Scientific) (to mark blood vessels); rat anti-BrdU (1:200, Ab6326, Abcam); rabbit anti-Fibrinogen (1:100, A0080, Dako); and rabbit anti-Pdgfr- β (1:100, 28E1, Cell Signaling Technology).

To determine pericyte blood vessel coverage in the rostral hypothalamus, the linear surface area stained with anti-Pdgfr- β antibodies (for pericytes) was divided by the area stained with anti-Glut-1 antibodies (for blood vessels) in three p35-42 *Gfap-Cre^{ERT2};Smo^{-/-}*, three *Aldh1l1-Cre^{ERT2};Smo^{-/-}*, and six control mice treated with TAMX.

For TJ protein staining, mice were perfused in PBS and then flash frozen in OCT (Tissue-Tek). Tissues (brain or spinal cord) were cut at 20 μ m and mounted on Superfrost Plus slides. Sections were fixed with 95% ethanol (30 min) and acetone (1 min) prior to applying primary antibodies. The following antibodies were used: rabbit anti-ZO-1 (1:50; 40-2300), Claudin-5 (1:100, 4C3C2), and Occludin (1:100; 71-1500) (all obtained from Thermo Fisher Scientific).

Albumin Leakage Quantification. For image acquisition, we first established exposure parameters by visualizing extravasation in the median eminence or arcuate nucleus in controls, which were then kept constant for all images captured in control and experimental animals. Alexa488-albumin leakage was quantified in captured images using Fiji (ImageJ) software as follows: the albumin channel was first auto-thresholded to determine the total area of leakage, and areas that exceeded the threshold levels were scored by determining average pixel intensity in the field of view (at 20 \times objective) for single image z-planes. Intensity values were collected from 5 to 10 individual sections captured at the same exposure settings from 3 to 5 different mice per experiment. Individual intensity data values are plotted in Fig. 2 E and F.

Western Blotting. Tissue samples (including spinal cord, hypothalamus, and cortex) were collected from P35-42 experimental mice on day 4 following 3 successive days of receiving a single TAMX injection and lysed on ice in lysis buffer Tissue Protein Extraction Reagent mixed with protease inhibitor mixture (Thermo Scientific). The cell lysate was cleared by centrifugation at 6,600 \times g at 4 °C for 10 min and collected in 1.5 mL Eppendorf tubes. Protein concentration was determined and normalized into 5 μ g/ μ L using Pierce 660 nm Protein Assay Reagent (Thermo Fisher) on a Spectronic Genesys 5 spectrophotometer. A certain amount of protein samples (spinal cord 20 μ g, hypothalamus 30 μ g, cortex 50 μ g) were mixed with NuPAGE Sample Reducing Agent and LDS Sample Buffer (Thermo Scientific) and then heated for 10 min at 95 °C. The protein analysis applied with NuPAGE 4% to 12% Bis-Tris Gels (Thermo Scientific) at 100 V about 2 h and then wet blot transferred (30 V for 80 min) onto nitrocellulose membranes (GVS Life Sciences).

The membranes were incubated at room temperature for 4 h in blocking buffer with 5% milk, nonfat powdered (VWR), 10% fetal bovine serum (fetal bovine serum [FBS]; Sigma), and 0.04% Triton X-100 (Thermo Scientific) in PBS. Membranes were incubated overnight at 4 °C with the following primary antibodies: mouse anti-GAPDH (1:5,000, MAB374, EMD Millipore); rabbit anti-Pdgfr- β (1:1,000, 28E1, Cell Signaling Technology); rabbit anti-Caveolin1 (1:300, Ab18199, Abcam); and rabbit anti-GFAP (1:1,000, Z0334, Dako). For TJ staining, the primary antibodies listed in *Immunohistochemistry* were used at 1:500. After three washes with PBST (0.04% Triton X-100 in PBS), horseradish peroxidase-conjugated secondary antibodies were applied for 1 h at room temperature. Blots were developed with WesternBright ECL HRP Substrate (K-12045-D20, Advanta) and

visualized using G:BOX iChemIXR (Syngene). Quantification of band intensity were performed using ImageJ or Fiji. The relative levels of target proteins were normalized to GAPDH levels on the same blot.

RT-PCR. Quantitative real-time PCR (qRT-PCR): ~8-wk-old C57BL/6J mice (000664, the Jackson Laboratory) were treated with cyc at 20 mg/kg body weight or equal volume of 45% HPBC vehicle solution as controls. Twenty-four hours later, spinal cord, diencephalon, and cortex tissues were collected. Total RNA was extracted using TRIzol reagent (15596026 Thermo Fisher). Briefly, each tissue was cut into small pieces and homogenized in 1 mL of TRIzol reagent. Chloroform was applied to purify the aqueous phase for two rounds. RNA was precipitated with 0.5 mL isopropanol and 5 μ g of glycogen (R0551 Thermo Fisher). Pellet was further washed with 75% ethanol, air dried for 10 min, and resuspended in 20 μ L Molecular Biology Grade water (46-000-CV Corning) supplemented with 1 μ L or 40 U RNaseOUT (10777-019 Invitrogen). Next, the potential contaminating genomic DNA was removed from RNA preparations using TURBO DNA-free kit (AM1907 Ambion). Briefly, RNA solution was added with 1 μ L of TURBO DNase, 1.5 μ L of RNaseOUT, 5 μ L DNase Buffer, and Molecular Biology Grade water to setup a 50 μ L reaction. DNase was further inactivated using 5 μ L of DNase Inactivation Reagent. After DNA removal, 2 μ g RNA from each sample was used to perform reverse transcription with Oligo(dT) primer and M-MLV Reverse Transcriptase (M1701 Promega). qRTs were performed on Applied Biosystems StepOne Real-Time PCR system with StepOne v2.1 software as previously described (47). Primer sequences used were *Gli1* forward CCAAGCCAACTTATGTACAGG; *Gli1* reverse AGCCCCCTCTTTGTTAATTGA (47); *Smo* forward TCAGCATGTACCAAGATGG; *Smo* reverse AAACGCTTCTTAAGTCTGGG (48); *GAPDH* (internal control) forward GGCCTTCGTGTTCTCTAC; and *GAPDH* reverse TGTATCATACTTGGCAGGTT. The 20 μ L qRT reactions were set up using iTaQ Universal SYBR Green Supermix system (172-5120 Bio-Rad).

Fluorescent-Activated Cell Sorting.

Spinal Cord GFP+, TdT+, and cortical TdT+ cell purification (Fig. 1 C and D). To isolate Gli1-expressing CNS cells, *Gli1-Cre^{ERT2};Rosa26^{eYFP}* mice were treated with TAMX (150 mg/kg body weight) once per day for three continuous days at ~P35. At ~P49, spinal cord tissue was collected on ice, minced with forceps into a slurry, suspended in a 0.05% Trypsin-EDTA solution (35-052-CI, Cellgro), and incubated at 37 °C in a CO₂-balanced incubator for 20 min. DMEM (11995-040, Thermo Scientific) with 10% FBS (059K03621 Sigma) and DNase I (18047019, Thermo Scientific) were added to the cell suspension, followed by filtering through a sterile 40 μ m nylon mesh (22363547, Fisher Scientific) to remove the nondissociated tissue. Cells were centrifuged, resuspended, and repelleted using DMEM with 10% FBS and then Hepes buffer (1 \times PBS [Ca²⁺, Mg²⁺ free], 25 mM Hepes solution (H0887-20 mL, Sigma), and 1% FBS). Cell pellets were finally resuspended in ~1 mL ice cold Hepes buffer at a concentration of ~3 million cells/mL and transferred into tissue 12 \times 75 round bottom polypylene tubes (352063, BD Falcon). eYFP-expressing (Gli1+) cells were then sorted on a MoFlo XDP Cell Sorter (Beckman Coulter), while TdT-expressing cells were isolated on a BD Biosciences Influx High Speed Cell Sorter. *Gli1-Cre^{ERT2};Rosa26^{TdTTdT}* mice were treated with TAMX (150 mg/kg body weight) per day for three continuous days at ~P35. At ~P49, cortex and spinal cord tissue was dissected and transferred into gentleMACS C-Tubes (130-093-237, Miltenyi Biotec) with Enzyme Mix 1 from Neural Tissue Dissociation Kit (P) (130-092-628, Miltenyi Biotec) and then dissociated using the gentleMACS Dissociator (130-093-235, Miltenyi Biotec). To remove the nondissociated tissue, cell suspensions were filtered with MACS SmartStrainer 30 μ m (130-098-458, Miltenyi Biotec). Cells were pelleted and then the Debris Removal Solution Kit (130-109-398, Miltenyi Biotec) was used to cleanup myelin debris. TdT-expressing (Gli1+) cells were then isolated on a BD Biosciences Influx High Speed Cell Sorter.

Bulk RNAseq. Fluorescently labeled Gli1+ cells, sorted from spinal cord or cortex were sent to Admera Health LLC to perform RNAseq. RNA was extracted using the RNeasy Plus Micro Kit (74034, Qiagen). Complementary DNA libraries were constructed using the SMART-Seq v4 Ultra Low Input RNA Kit (Takara-Clontech). Final library quantity was evaluated with KAPA SYBR FAST qPCR and TapeStation RNA HS Assay (Agilent Technologies). Libraries were pooled in equimolar ratios and sequenced on the Illumina HiSeq platform (Illumina). Sequencing data were first aligned to mouse reference genomes using STAR mapping tool and then read counts were quantified using HTSeq-count.

EM Imaging and Quantification. Animals were perfused transcardially with 2.5% glutaraldehyde in 0.1 M PBS. Tissues were harvested and fixed overnight in the same fixative prior to vibratome sectioning at 70 μ m. The rostral hypothalamus and gray matter of the spinal cord were dissected and

underwent postfixation with 1.0% osmium tetroxide for 2 h. Dissected tissues were negatively stained with uranyl acetate for 30 min according to Palay's method. Tissues were then dehydrated by graded immersion in 50%, 70%, 95%, and 100% ethanol for 3 to 5 min each. Ethanol was then cleared from the tissues with acetone. The tissues were embedded in epoxy resin and polymerized at 65 °C for 48 h. Thick (1 μ m) and thin (0.13 to 0.15 μ m) sections were cut on an ultramicrotome, and thin sections were collected on carbon-coated copper grids for imaging. Images were collected on a Philips CM12 scanning transmission electron microscope. The number of vesicles present in each 1 μ m of linear distance along the EC circumference was scored for wild type (W7) and experimental mice (three in each category). To quantify mitochondria, we scored the number of discrete organelles identified as mitochondria based on their characteristic morphology within each 1- μ m length of EC membrane. Finally, the circumference of each EC used in these analyses was determined by direct measurement from 8,000 \times magnification images.

Image Processing and Statistical Analysis. All immunofluorescent images were captured on an Olympus FV-1,000 Scanning Confocal Microscope except Fig. 1A, which was captured on a Leica DMR-XA compound fluorescent microscope at 4 \times . All images were taken with 10 \times , 20 \times (air), or 60 \times (water

immersion) PlanApo fluorescent lenses with excitation laser intensities set to $\leq 15\%$. Raw single channel confocal images were captured in Fluoview FV-1,000 image capture software FV10-ASW (ver 4.2b) in ".oib" format and processed in Fiji software to generate color RGB composites in JPEG format. Some images were also processed in Adobe Photoshop Elements to adjust contrast, brightness, and sharpness (unsharp mask) for display. Figure composites were assembled and labeled in QuarkXPress 2018. Statistical analysis was performed in Microsoft Excel for Mac (version 16.39) or GraphPad Prism8 software. Unpaired two-tailed Student's *t* test was used for all comparisons.

Data Availability. Anonymized RNAseq data have been deposited in BioProject ([PRJNA681591](https://www.ncbi.nlm.nih.gov/bioproject/PRJNA681591)).

ACKNOWLEDGMENTS. This work was funded by a grant from the National Multiple Sclerosis Society (Grant RG-1803-30494) to M.P.M. and National Natural Science Foundation of China (Grant 31500845) to H.W. We gratefully acknowledge the generous assistance of W. Geoffrey McAuliffe with EM imaging and Dritan Aggaliiu with tail vein tracer injections as well as all of the investigators who shared reagents with us.

1. B. Broux, E. Gowing, A. Prat, Glial regulation of the blood-brain barrier in health and disease. *Semin. Immunopathol.* **37**, 577–590 (2015).
2. N. J. Abbott, L. Rönnebeck, E. Hansson, Astrocyte-endothelial interactions at the blood-brain barrier. *Nat. Rev. Neurosci.* **7**, 41–53 (2006).
3. C. P. Profaci, R. N. Munji, R. S. Pulido, R. Daneman, The blood-brain barrier in health and disease: Important unanswered questions. *J. Exp. Med.* **217**, e20190062 (2020).
4. R. Daneman, A. Prat, The blood-brain barrier. *Cold Spring Harb. Perspect. Biol.* **7**, a020412 (2015).
5. M. D. Sweeney, Z. Zhao, A. Montagne, A. R. Nelson, B. V. Zlokovic, Blood-brain barrier: From physiology to disease and back. *Physiol. Rev.* **99**, 21–78 (2019).
6. S. Biswas, A. Cottarelli, D. Agalliu, Neuronal and glial regulation of CNS angiogenesis and barrierogenesis. *Development* **147**, dev182279 (2020).
7. S. Liebner *et al.*, Functional morphology of the blood-brain barrier in health and disease. *Acta Neuropathol.* **135**, 311–336 (2018).
8. S. Michinaga, Y. Koyama, Dual roles of astrocyte-derived factors in regulation of blood-brain barrier function after brain damage. *Int. J. Mol. Sci.* **20**, 571 (2019).
9. R. Cabezas *et al.*, Astrocytic modulation of blood brain barrier: Perspectives on Parkinson's disease. *Front. Cell. Neurosci.* **8**, 211 (2014).
10. M. V. Sofroniew, Astrocyte barriers to neurotoxic inflammation. *Nat. Rev. Neurosci.* **16**, 249–263 (2015).
11. R. Daneman, The blood-brain barrier in health and disease. *Ann. Neurol.* **72**, 648–672 (2012).
12. B. Obermeier, R. Daneman, R. M. Ransohoff, Development, maintenance and disruption of the blood-brain barrier. *Nat. Med.* **19**, 1584–1596 (2013).
13. L. Morel *et al.*, Molecular and functional properties of regional astrocytes in the adult brain. *J. Neurosci.* **37**, 8706–8717 (2017).
14. L. Morel *et al.*, Intracortical astrocyte subpopulations defined by astrocyte reporter Mice in the adult brain. *Glia* **67**, 171–181 (2019).
15. S. A. Liddelow, B. A. Barres, Reactive astrocytes: Production, function, and therapeutic potential. *Immunity* **46**, 957–967 (2017).
16. S. A. Liddelow *et al.*, Neurotoxic reactive astrocytes are induced by activated microglia. *Nature* **541**, 481–487 (2017).
17. Y. Zhang *et al.*, An RNA-sequencing transcriptome and splicing database of glia, neurons, and vascular cells of the cerebral cortex. *J. Neurosci.* **34**, 11929–11947 (2014).
18. J. D. Cahoy *et al.*, A transcriptome database for astrocytes, neurons, and oligodendrocytes: A new resource for understanding brain development and function. *J. Neurosci.* **28**, 264–278 (2008).
19. J. L. Zamanian *et al.*, Genomic analysis of reactive astrogliosis. *J. Neurosci.* **32**, 6391–6410 (2012).
20. A. Zeisel *et al.*, Molecular architecture of the mouse nervous system. *Cell* **174**, 999–1014.e22 (2018).
21. M. Vanlandewijck *et al.*, A molecular atlas of cell types and zonation in the brain vasculature. *Nature* **554**, 475–480 (2018).
22. M. Blanchette, R. Daneman, Formation and maintenance of the BBB. *Mech. Dev.* **138**, 8–16 (2015).
23. P. Polakis, Formation of the blood-brain barrier: Wnt signaling seals the deal. *J. Cell Biol.* **183**, 371–373 (2008).
24. A. D. Garcia, R. Petrova, L. Eng, A. L. Joyner, Sonic hedgehog regulates discrete populations of astrocytes in the adult mouse forebrain. *J. Neurosci.* **30**, 13597–13608 (2010).
25. R. V. Allahyari, K. L. Clark, K. A. Shepard, A. D. R. Garcia, Sonic hedgehog signaling is negatively regulated in reactive astrocytes after forebrain stab injury. *Sci. Rep.* **9**, 565 (2019).
26. Y. G. Han *et al.*, Hedgehog signaling and primary cilia are required for the formation of adult neural stem cells. *Nat. Neurosci.* **11**, 277–284 (2008).
27. V. Palma *et al.*, Sonic hedgehog controls stem cell behavior in the postnatal and adult brain. *Development* **132**, 335–344 (2005).
28. T. Tenzen *et al.*, The cell surface membrane proteins Cdo and Boc are components and targets of the hedgehog signaling pathway and feedback network in mice. *Dev. Cell* **10**, 647–656 (2006).
29. B. L. Allen, T. Tenzen, A. P. McMahon, The hedgehog-binding proteins Gas1 and Cdo cooperate to positively regulate Shh signaling during mouse development. *Genes Dev.* **21**, 1244–1257 (2007).
30. O. R. Yabut, S. J. Pleasure, Sonic hedgehog signaling rises to the surface: Emerging roles in neocortical development. *Brain Plast.* **3**, 119–128 (2018).
31. C. B. Bai, D. Stephen, A. L. Joyner, All mouse ventral spinal cord patterning by hedgehog is Gli dependent and involves an activator function of Gli3. *Dev. Cell* **6**, 103–115 (2004).
32. Q. Lei, A. K. Zelman, E. Kuang, S. Li, M. P. Matisse, Transduction of graded hedgehog signaling by a combination of Gli2 and Gli3 activator functions in the developing spinal cord. *Development* **131**, 3593–3604 (2004).
33. H. L. Park *et al.*, Mouse Gli1 mutants are viable but have defects in SHH signaling in combination with a Gli2 mutation. *Development* **127**, 1593–1605 (2000).
34. F. Long, X. M. Zhang, S. Karp, Y. Yang, A. P. McMahon, Genetic manipulation of hedgehog signaling in the endochondral skeleton reveals a direct role in the regulation of chondrocyte proliferation. *Development* **128**, 5099–5108 (2001).
35. Y. M. Ganat *et al.*, Early postnatal astroglial cells produce multilineage precursors and neural stem cells in vivo. *J. Neurosci.* **26**, 8609–8621 (2006).
36. Y. M. Park, H. Chun, J. I. Shin, C. J. Lee, Astrocyte specificity and coverage of hGFAP-CreERT2 [Tg(GFAP-Cre/ERT2)13Kdmc] mouse line in various brain regions. *Exp. Neurol.* **27**, 508–525 (2018).
37. R. Srinivasan *et al.*, New transgenic mouse lines for selectively targeting astrocytes and studying calcium signals in astrocyte processes in situ and in vivo. *Neuron* **92**, 1181–1195 (2016).
38. J. K. Chen, J. Taipale, M. K. Cooper, P. A. Beachy, Inhibition of hedgehog signaling by direct binding of cyclopamine to smoothened. *Genes Dev.* **16**, 2743–2748 (2002).
39. M. M. Boisvert, G. A. Erikson, M. N. Shokhirev, N. J. Allen, The aging astrocyte transcriptome from multiple regions of the mouse brain. *Cell Rep.* **22**, 269–285 (2018).
40. M. Pekny, M. Pekna, Reactive gliosis in the pathogenesis of CNS diseases. *Biochim. Biophys. Acta* **1862**, 483–491 (2016).
41. J. E. Burda, M. V. Sofroniew, Reactive gliosis and the multicellular response to CNS damage and disease. *Neuron* **81**, 229–248 (2014).
42. A. Alvarez-Buylla, R. A. Ihrie, Sonic hedgehog signaling in the postnatal brain. *Semin. Cell Dev. Biol.* **33**, 105–111 (2014).
43. J. I. Alvarez *et al.*, The hedgehog pathway promotes blood-brain barrier integrity and CNS immune quiescence. *Science* **334**, 1727–1731 (2011).
44. T. K. Rimkus, R. L. Carpenter, S. Qasem, M. Chan, H. W. Lo, Targeting the sonic hedgehog signaling pathway: Review of smoothened and Gli inhibitors. *Cancers (Basel)* **8**, 22 (2016).
45. S. Ahn, A. L. Joyner, Dynamic changes in the response of cells to positive hedgehog signaling during mouse limb patterning. *Cell* **118**, 505–516 (2004).
46. C. B. Bai, W. Auerbach, J. S. Lee, D. Stephen, A. L. Joyner, Gli2, but not Gli1, is required for initial Shh signaling and ectopic activation of the Shh pathway. *Development* **129**, 4753–4761 (2002).
47. P. Niewiadomski, R. Rohatgi, Measuring expression levels of endogenous Gli genes by immunoblotting and real-time PCR. *Methods Mol. Biol.* **1322**, 81–92 (2015).
48. W. T. Farmer *et al.*, Neurons diversify astrocytes in the adult brain through sonic hedgehog signaling. *Science* **351**, 849–854 (2016).